Journal of Materials Chemistry A

PAPER

View Article Online
View Journal | View Issue

Cite this: J. Mater. Chem. A, 2019, 7, 9890

Rational design and kinetics study of flexible sodium-ion full batteries based on binder-free composite film electrodes †

Keliang Zhang,[a] Xudong Zhang,*[a] Wen He,*[a] Wangning Xu,[a] Guogang Xu,[b] Xinli Yi,[a] Xuena Yang[a] and Jiefang Zhu*[c]

A high-performance flexible sodium-ion full battery (FSIFB) is developed by using binder-free composite film (BFCF) electrodes without using conductive carbon and current collectors. Hard carbon fibers decorated with different electrochemical active materials are used as the supporting framework and 3D conductive network of FSIFBs for the first time. Different pre-sodiated anodes and the electrolyte additives are designed for well-matched FSIFBs. Using a porous $Na_3V_2(PO_4)_3$ coated hard carbon fiber film with a mass loading of 2.34 mg cm^{-2} as the cathode and a pre-sodiated graphene/SiC/hard carbon fiber film with a mass loading of 1.50 mg cm^{-2} as the anode, an optimized FSIFB is designed. It delivers high output voltage (3.34 V), high energy density (234.1 W h kg^{-1} at a high-current rate of 0.5 A g^{-1}), ultralong cyclability (over 2905 cycles at 0.5 A g^{-1} and 1000 cycles at 5 A g^{-1}), and high coulombic efficiency (approaching 100%), which surpasses those of all FSIFBs reported so far. Furthermore, this FSIFB still maintains good electrochemical attributes even at serious bending states in water. The models of the solid electrolyte interphase behavior on the surface of electrodes in the FSIFB are studied by using EIS, and a reaction mechanism and an equivalent electrical circuit are proposed. We also provide the videos of the preparation process for a pouch-type FSIFB to demonstrate its simple operability and potential applications.

Received 26th January 2019
Accepted 19th March 2019

DOI: 10.1039/c9ta01026b

rsc.li/materials-a

1. Introduction

Developing new and low-cost technologies in environmentally friendly energy storage systems is a life-time goal for researchers.[1–5] With the rapidly increasing demand for versatile energy storage devices, great interest has been aroused in flexible/bendable electronic equipment, such as rollup displays, wearable and portable electronic devices and implantable biomedical products.[6–8] Nevertheless, flexible rechargeable batteries still suffer from the lack of advanced electrodes with high energy density, high reversible capacities, fast charge–discharge rates and a long lifespan. The design of a flexible battery usually requires light, flexible, and small units with shape-conformability, aesthetic diversity, and excellent mechanical properties.[9] However, traditional flexible electrode materials often suffer from low specific power density and other poor performances due to a certain amount of binder being added to improve their flexibility. Therefore, numerous research efforts have been directed to the design of flexible, binder-free, and thin-film electrodes. For instance, CNTs, graphene paper, carbon cloth or textiles, and composite materials have been used as flexible binder-free electrodes.[10–16] Despite these advances, the rational design of cheap flexible binder-free electrodes with high capacity and high energy density, fast charge–discharge rates and a long cycling lifetime remains a long-standing challenge.

Recently, sodium ion batteries (SIBs) for large-scale energy storage have been rapidly developed due to the abundance and low-cost of sodium resources, and have become the most promising alternative to lithium ion batteries (LIBs).[17–19] In particular, the investigation of cheap electrodes (such as TiO_2 nanotubes, hard carbon materials, electroactive organics/graphene composites, and so on) and safe polymeric electrolytes for SIBs has recently become a hot topic within the scientific community.[20–22] Bella *et al.* reported some polymer electrolytes for SIBs, showing a wide electrochemical stability window *versus* Na/Na^+ and stable long-term constant-current charge/discharge cycling.[23,24] However, the energy density, charge–discharge rate and cycling lifetime of the electrode materials are extremely important for SIBs, which have been seriously limited by the intrinsic high potential of Na, large

[a]College of Material Science and Engineering, Qilu University of Technology (Shandong Academy of Sciences), Jinan 250353, China. E-mail: zxd1080@126.com
[b]College of Material Science and Engineering, Shandong University of Science and Technology, Qingdao 266590, China
[c]Department of Chemistry-Ångström Laboratory, Uppsala University, Box 538, SE-75121 Uppsala, Sweden

† Electronic supplementary information (ESI) available. See DOI: 10.1039/c9ta01026b

ionic size of Na ions and high polarization of electrodes.[25] Thus, the rational design and fabrication of high-voltage cathodes with suppressed polarization and well-matched anodes are key for the development of high-performance sodium-ion full batteries (SIFBs).[26] In addition, the research studies on flexible SIFBs are in the beginning stage, and the electrochemical performances remain unsatisfactory due to the low chemical reaction kinetics for Na ion insertion. Therefore, the process control of well-matched SIFBs is also important and needs to be investigated.

A polyanion-type compound with a highly open 3D framework structure and high Na-transport/reaction kinetics, such as $Na_3V_2(PO_4)_3$ (NVP), can supply large and interconnected vacant sites, and build suitable paths for the diffusion of Na ions.[27–32] In particular, NVP has high potential plateaus at 3.4 V, and it can be used as an ideal cathode material of SIFBs. Yu *et al.* reported that interconnected 3D NVP/C composites delivered superior rate capability and excellent cycling stability, but the exploration of a suitable counter electrode *vs.* NVP to fabricate high-performance SIFBs still remains unsatisfactory.[33] Xia *et al.* reported an interesting flexible SIFB using NVP/C@rGO composites as both the cathode and anode.[27] The reported cell exhibited good electrochemical performance, with 1.7 V as the output voltage plateau and a capacity of 74.1 mA h g^{-1} at 0.5C. However, its lower voltage plateau results in lower energy density. Among anode materials for SIBs, such as carbonaceous materials,[34,35] metal oxides/sulfides,[36] *etc.*, hard carbon (HC) has a favorable Na cation storage capacity (250–300 mA h g^{-1}), good rate capability (up to 10C) and a median voltage of 0.1 V.[37–43] In particular, the NVP/HC electrode system possesses a high theoretical operating voltage at 3.3 V, which further endows it with great potential to be used as a cathode for high-energy and low-cost SIFBs.[44,45] Liqiang Mai *et al.*[46] reported a SIFB based on a NASICON structured NVP cathode and poorly graphitized hard carbon anode, which exhibited a theoretical average voltage of 3.3 V and a substantial increase in the energy density (>20%) compared to bulk and bare NVP based full cells.

Here, we report a high-performance flexible sodium-ion full battery (FSIFB). This FSIFB is assembled with binder-free composite film (BFCF) electrodes prepared at 800 °C without using conductive carbon and current collectors. Carbonized filter paper fibers decorated with different electrochemical active materials are used as hard carbon fibers, a flexible supporting framework and a 3D conductive network of the composite film electrodes. The different pre-sodiated anodes and the electrolyte additives are designed for well-matched FSIFBs. The challenge of this design is to retain efficient Na ion diffusion in cathode and anode electrodes simultaneously and thus, achieving ultralong cycle ability at a fast charging/discharging rate. Several merits of this FSIFB design are as follows: (1) compared with other flexible supporting framework materials, such as carbonized cellulose and polyvinylidene fluoride, reduced graphene oxide (rGO), graphene foam (GF), carbon fiber cloth (CFC), carbon cloth (CC), and stainless steel cloth (ESI Tables S1 and S2†), the hard carbon fibers (HCFs) from carbonized filter paper as a supporting framework material of FSIFBs show unique advantages, such as low cost, simple and scalable preparation method, high carbon content and surface area, chemical functionalization, well flexibility and conductivity, shape diversity, light weight, non-toxicity, unique morphology, good coordination between the cathode and anode and recyclability; (2) the HCF increases the active constituent part, charge reaction and Na^+ storage sites of NVP, directly resulting in a significant improvement of the Na^+ transportation and the conductivity of the composite cathode; (3) the flexible cross-linked porous framework of HCF and the porous structure of NVP in the BFCF-NVP/HCF not only are favourable for Na^+ insertion/desertion during the charging/discharging processes, but also offer an elastic buffer to accommodate the volume change of NVP, resulting to an excellent cycle performance; (4) being free of an insulating binder and other additives, avoiding "dead volume" within the electrode; (5) porous NVP coated highly conductive HCFs for improving transport of Na^+ and electrons; (6) a HCF core/NVP shell structure for helping electron transport and Na^+ migration in BFCF; (7) the pre-sodiated anodes and the electrolyte additives designed for improving electrical transport behaviours and the dynamics of FSIFBs; and (8) an aluminum–plastic film used as a flexible water-proof case for the FSIFBs, showing superior water-proofing function. The aim of this study highlights the enormous potential of FSIFBs in versatile flexible and wearable applications.

2. Experimental

2.1 Material synthesis

2.1.1 Synthesis of the NVP precursor. The NVP precursor was synthesized by a sol–gel procedure. Firstly, NH_4VO_3 (99%, Tianjin Bodi Chemical Co. Ltd.) and citric acid (99.5%, Tianjin Bodi Chemical Co. Ltd.) with a stoichiometric molar ratio of 2 : 2 were dissolved in deionized water and stirred for 0.5 h. Secondly, 0.0075 M NaOH (95%, Tianjin Bodi Chemical Co. Ltd.) and 0.0075 M $NH_4H_2PO_4$ (99%, Tianjin Bodi Chemical Co. Ltd.) were added into another beaker and stirred for 0.5 h. Lastly, the above solutions were mixed together and the mixed solution was heated and evaporated at 70 °C. The resulting gel was dried at 120 °C. The obtained dark green precursor was sintered in two steps at 350 °C for 4 h and then at 800 °C for 8 h under a N_2 atmosphere.

2.1.2 Synthesis of BFCF-NVP/HCF cathodes. A filter paper was used as a support material. Firstly, the filter paper was spread on a glass plate and an appropriate amount of hydrazine hydrate was dripped onto the filter paper, then it was covered with another glass plate. Subsequently, it was dried at 120 °C for 12 h. Second, an appropriate amount of NVP precursor was dispersed in *N*-methylpyrrolidone (NMP) to form a slurry. Then the slurry was coated on the filter paper after processing. The coating thickness is 100, 150 and 200 μm, respectively. Owing to the 3D porous structure of filter paper, the slurry easily penetrated into it. Then, the filter paper coated with the slurry was dried at 60 °C. The final samples were punched into discs with a diameter of 14.0 mm and were sintered at different temperatures (700, 750 and 800 °C) for 6 h, 8 h and 10 h in a N_2 atmosphere to form BFCF-NVP/HCF cathodes.

2.1.3 Synthesis of different anodes. The graphene/SiC nanocomposite (GN/SiC) sample was prepared following our previously reported method.[47] The treatment method of filter paper was the same as in the first step for the synthesis of the BFCF-NVP/HCF cathodes. The preparation method of GN/SiC/HCF and the PGN/SiC/HCF anodes can be seen in ESI Fig. S1.† The $NaVOPO_4$ anode was synthesized by using adenosine triphosphate (ATP) templates. First, 1.2 mmol ATP was added to 50 ml distilled water in a 70 °C water-bath, which formed solution A. Then, 2.4 mmol NH_4VO_3 and 0.9 mmol ascorbic acid were added to 50 ml distilled water, which was stirred for 20 minutes to form solution B. Finally, solutions A and B were mixed together, which was transferred to a 100 ml Teflon-lined autoclave and kept at 100 °C for 21 h. Subsequently, the brown mixture from hydrothermal treatment was dried at 80 °C for 12 h to form a xerogel. The xerogel was sintered at 350 °C for 4 h and then at 800 °C for 12 h under a N_2 atmosphere.

2.2 Characterization

The characterization methods of samples can be seen in ESI S4.†

2.3 Electrochemical evaluation

The electrochemical properties of the BFCF electrodes were tested after assembling coin-type cells (CR2032) in a glove box filled with pure argon. For the half-cell test, sodium metal was used as the counter and the reference electrode, a solution of 1 M $NaClO_4$ in EC : PC (1 : 1, v/v) or 1 M $NaClO_4$ in EC : PC (1 : 1, v/v) + 5% FEC as the electrolyte, and a Whatman glass microfiber filter (Grade GF/F) as the separator. For pouch-type FSIFBs, BFCF-NVP/HCF was used as the cathode and different electrodes as anodes, and a flexible water-proof case made of aluminum-plastic film (DNP, Japan) was used. The battery was aged for 12 h before testing to ensure full absorption of the electrolyte into the electrodes. Galvanostatic charge/discharge measurements were performed with a Channels battery analyzer (CT3008W). Electrochemical impedance spectroscopy (EIS) and cyclic voltammetry (CV) measurements were performed on a PARSTAT 2263 electrochemical workstation. EIS were recorded with frequencies ranging from 100 kHz to 10 MHz with an AC signal of 5 mV amplitude as the perturbation. The voltage range of CV measurements was 2.0–4.3 V and the scan rate was from 0.1 to 0.6 mV s^{-1}. All the tests were performed at room temperature.

We also provide the videos of the fabrication process for the pouch-type FSIFBs with a superior water-proof case to demonstrate the simple operability and potential applications of FSIFBs (vitro S1, see ESI S5†).

3. Results and discussion

3.1 Electrochemical performances of the pouch-type FSIFBs

Using the binder-free composite film (BFCF) electrodes without using conductive carbon and current collectors, pouch-type FSIFBs were assembled and tested with a mass ratio of cathode/anode of about 2.56. To demonstrate the application of FSIFBs assembled with the BFCF-NVP/HCF cathode and the PGN/SiC/HCF anode, they were used to power a commercial red light-emitting diode (LED) (2.4 V, 0.3 W). The schematic illustration for their fabrication and microstructure is shown in Fig. 1a, showing electron transport and Na ion diffusion in the HCF core/NVP shell structure. Fig. 1b shows the schematic diagram of the FSIFB, showing that it lit up 7 LED lamps. To prove that it is a "flexible" battery, the flexibility of the cell was tested. The lit LED bulb driven by the FSIFB after different bending cycles at a bending angle of 30–90° demonstrates different luminosities (ESI Fig. S2†). As demonstrated in Fig. 1c, d and Video S2 of ESI S5,† a LED bulb can also be powered even when the battery was bent after 1600 cycles. No electrical failure was observed during the bending process of the cell. Fig. 1c shows that the luminosity of the LED lamp is still present even after the cell had been severely bent. Fig. 1e shows that there was no leakage when the cell was severely bent in water, see Video S2 of ESI S5.† What's more, when the pouch-type FSIFB after 1600 bending cycles was disassembled, its BFCF-NVP/HCF cathode at different bending angles was still intact (ESI Fig. S3 and Video S2, ESI S5†). The results show that the FSIFB has good flexibility, similar to studies on flexible batteries.[48,49]

Fig. 2 shows the sodium storage performances of the pouch-type FSIFBs assembled with the BFCF-NVP/HCF cathode and the different anodes at different current rates of the cathode (Table S3†). The charge/discharge curves of the FSIFBs are illustrated in Fig. 2a. Compared with the pre-sodiated HCF (PHCF) and $NaVOPO_4$ anodes, the FSIFB assembled with the PGN/SiC/HCF anode not only exhibits the highest output voltage of 3.34 V and lowest polarization, but the highest specific energy density, at 0.5 A g^{-1} reaching up to 234.1 W h kg^{-1} (Fig. 2b), much better than that of other SIBs reported in the literature (Table S2†). Fig. 2c shows the charge/discharge curves of the pouch-type FSIFB assembled with the BFCF-NVP/HCF cathode and the PGN/SiC/HCF anode at different current rates from 0.05 A g^{-1} to 20 A g^{-1}, exhibiting a small degree of polarization and the small decay of capacity at low current rates 0.05–0.5 A g^{-1}. In particular at ultrahigh current rates of 15 and 20 A g^{-1}, the discharge capacities still maintained at 51.7 and 27.7 mA h g^{-1}, respectively. Based on the above analysis, the electrochemical properties of the pouch-type FSIFBs, especially the rate capability and cycling stability, are significantly affected by the pre-sodiated anode, which can be facilely controlled *via* the fabrication process. The results show that the BFCF-NVP/HCF cathode is well matched with the PGN/SiC/HCF anode in this FSIFB. More importantly, this pouch-type FSIFB not only exhibits a high output voltage of 3.34 V, high energy density (234.1 W h kg^{-1} at 0.05 A g^{-1}) and high coulombic efficiency (approaching 100%), but also ultralong cyclability. Fig. 2d and e show the long-term cycling performances and coulombic efficiencies of the different FSIFBs (FSIFB-1 and FSIFB-2 for the repeated data that are further optimized) assembled with the BFCF-NVP/HCF cathode and the PGN/SiC/HCF anode, respectively. The initial specific capacities of FSIFB-1 and FSIFB-2 for repeated data are 81.87 and 88.93 mA h g^{-1} at 10 mA g^{-1}, respectively. Fig. 2d shows the

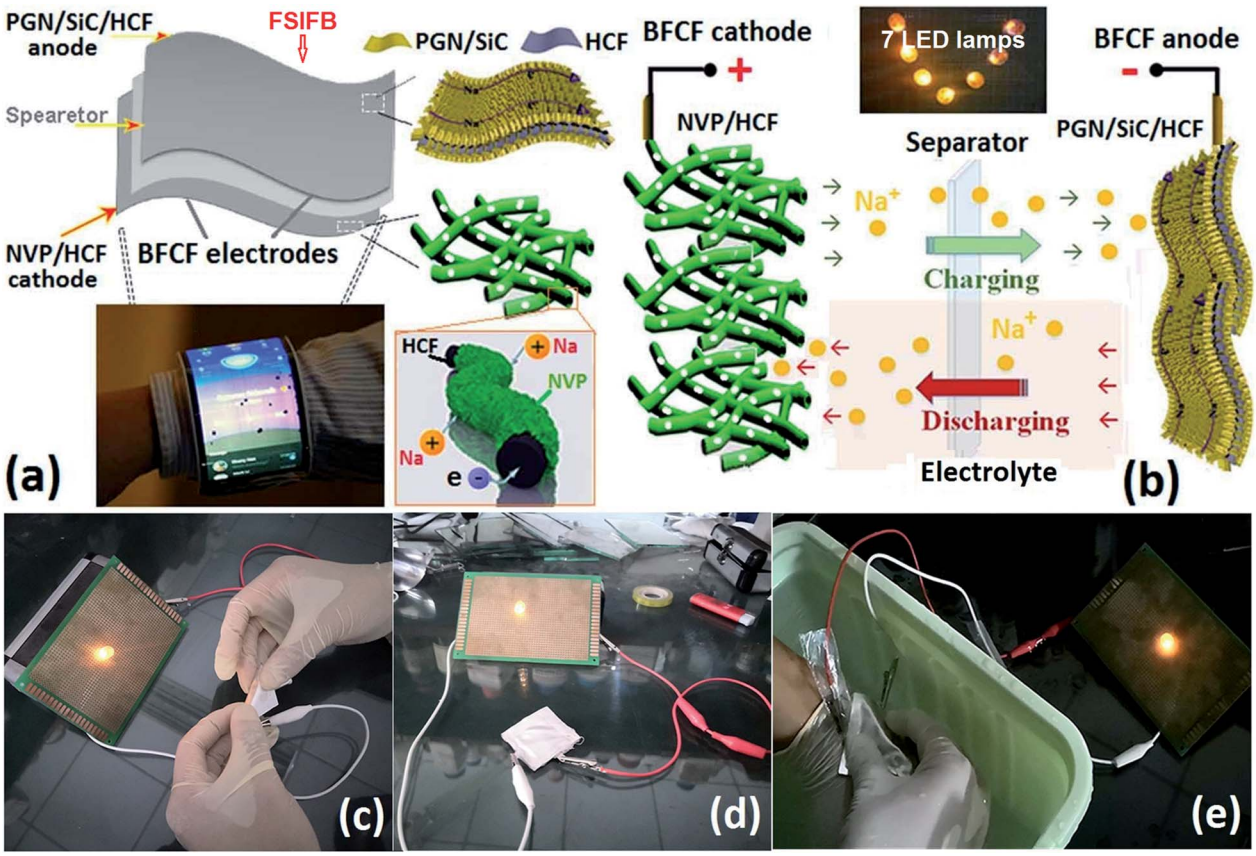

Fig. 1 (a) Schematic illustrations for the fabrication and microstructure of the flexible sodium-ion full battery (FSIFB) using the BFCF-NVP/HCF cathode and the PGN/SiC/HCF anode. (b) Schematic diagram of the FSIFB. (c) Photograph of the bended pouch-type FSIFB, almost no changes in the luminosity of the lit LED bulb driven by the FSIFB. (d) Photograph of the pouch-type FSIFB after bending. (e) Photograph of the bended pouch-type FSIFB in water.

long-term cycling stability (over 2905 cycles at 0.5 A g^{-1}) of the FSIFB-1, which corresponds to 0.42% capacity decay per cycle. Even after 1000 cycles at a high current rate of 5 A g^{-1}, the FSIFB-2 for repeated data could still display a specific discharge capacity of 30 mA h g^{-1} (Fig. 2e), but its cycle stability decreases due to its inherent low electrical conductivity of NVP, volumetric expansion/shrinkage during charge and discharge, and the solubility of the electrolyte.[50] These show unprecedented improvement in deformability and internal short-circuit prevention of cells, which offers great promise for next-generation versatile flexible electronics. The remarkably enhanced cycling stability and rate capability of this FSIFB are ascribed to the synergistic effects between the BFCF-NVP/HCF cathode and the PGN/SiC/HCF anode. The highly conductive HCF can act as the conductive core to provide efficient electron transport. The 3D macroporous architectures and the hierarchical nanostructures in BFCF can significantly facilitate the Na ion diffusion and enhance the contact area.

3.2 Na-migration kinetics study of the pouch-type FSIFBs

To explore the electrochemical performance and Na-migration kinetics of the FSIFBs assembled with the BFCF-NVP/HCF cathode and the different anodes, CV and EIS were performed. The CV curves of the FSIFBs assembled with the different anodes show significant differences in the electrochemical reactions (Fig. 3a). It is obvious that the FSIFBs assembled with the pre-sodiated HCF (PHCF) and the PGN/SiC/HCF anodes can exhibit an evident redox couple, which is associated with the reversible transformation of V^{3+}/V^{4+} accompanied by the insertion and extraction reaction of Na-ions from the NVP lattice matrix.[29] The oxidation peak and the corresponding reduction peak for the FSIFB assembled with the PGN/SiC/HCF anode are located at around 3.39 V and 3.12 V, respectively, showing stronger current intensity and smaller polarization than those of the FSIFBs assembled with other anodes. Fig. 3b shows the Nyquist plots of fresh FSIFBs assembled with the different anodes from 100 kHz to 0.01 Hz. They are composed of a semicircle at high-frequency and a long oblique line at low-frequency. According to a simple adsorption model,[51] the semicircle is related to the adsorption of Na ions from solvent on the particle surface of the electrode and charge balance, while the oblique line is related to the solid state diffusion of Na ions in the electrode. The insertion process of Na ions in a NVP/HCF single particle for the BFCF-NVP/HCF cathode is shown in Fig. 5b. The Na^+ insertion reaction contains a three-step process: (1) Na ions from the solvent are

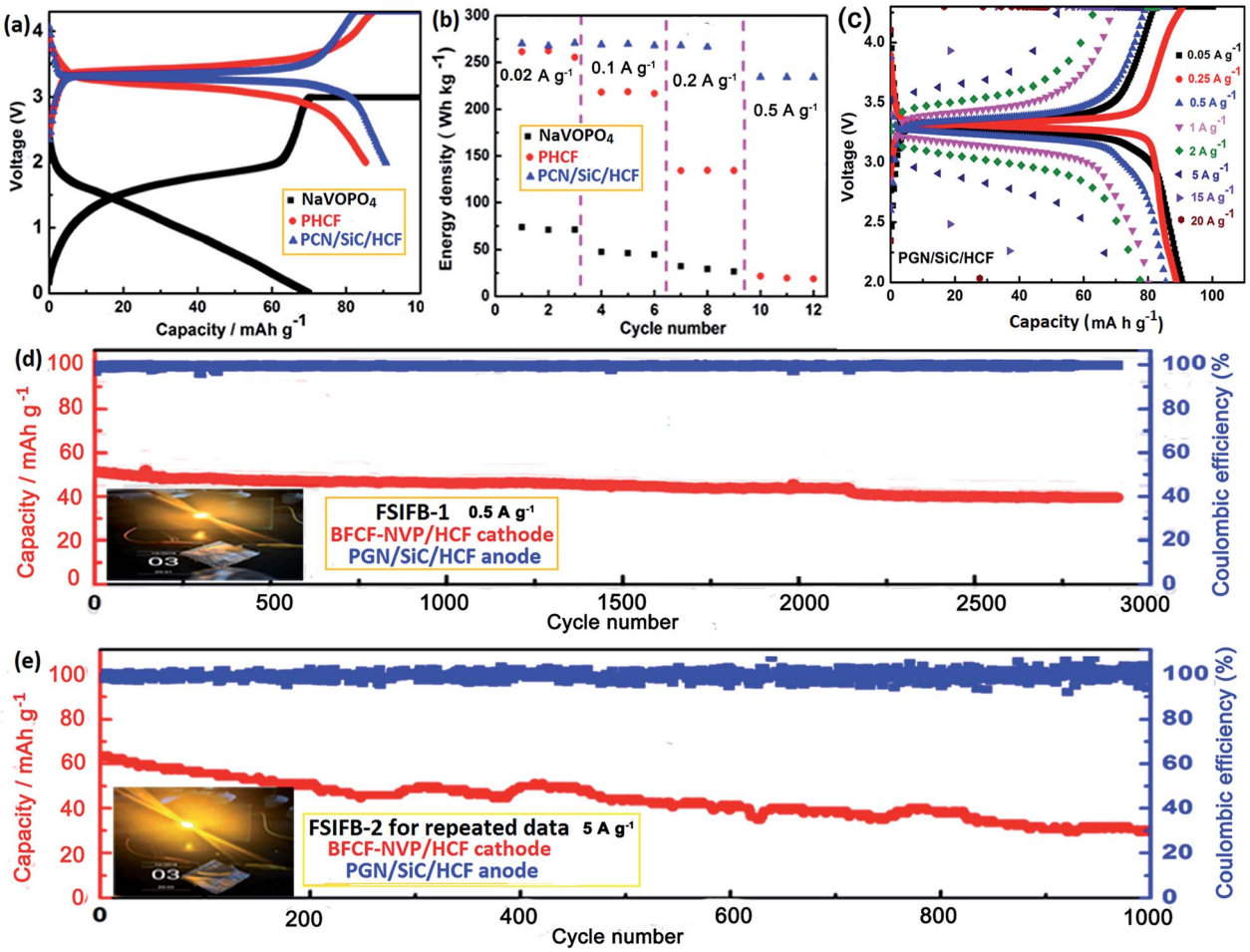

Fig. 2 Sodium storage performances of the pouch-type FSIFBs assembled with the BFCF-NVP/HCF cathode and the different anodes at different current rates of the cathode. (a) Galvanostatic charge/discharge curves of the FSIFBs assembled with the different anodes at a current rate of 10 mA g^{-1}. (b) Energy density comparison of the FSIFBs assembled with the different anodes at different current rates. (c) Galvanostatic charge/discharge curves of the FSIFB assembled with the BFCF-NVP/HCF cathode and the PGN/SiC/HCF anode at different current rates. Long-term cycling performances and coulombic efficiencies of the different FSIFBs assembled with the BFCF-NVP/HCF cathode and the PGN/SiC/HCF anode, (d) the FSIFB-1 at a current rate of 0.5 A g^{-1} and (e) the FSIFB-2 for the repeated data that are further optimized at 5 A g^{-1}.

adsorbed on the NVP/HCF particle surface; (2) electrons in HCF enter the valence bands of NVP and diffuse into the surrounding Na sites to make charges to balance; (3) finally, both the Na ions enter the lattice of NVP and the balancing electrons co-diffuse into the inside of NVP. The calculated value (219 Ω) of R_{ct} (charge transfer resistance) of the FSIFB assembled with the PGN/SiC/HCF anode is much smaller than that (1296 Ω) of the FSIFB assembled with the $NaVOPO_4$ anode, showing that the PGN/SiC/HCF anode plays an important role in making charge transfer easy.

The CV curves of the FSIFB assembled with the PGN/SiC/HCF anode at various scan rates are presented in Fig. 3c. With increasing scan rate, the oxidation and reduction peaks slightly move in positive and negative directions, respectively, revealing the good position repeatability of CV peaks and better electrochemical reversibility of the electrode reaction.[33] This phenomenon means larger polarization at high scan rates, which can be explained by the classical Randles–Sevcik method (eqn (1)).[52,53] Moreover, the diffusion coefficient (D, cm^2 s^{-1}) of sodium ions in different electrodes can also be calculated from eqn (1).

$$I_p = 2.69 \times 10^5 A n^{3/2} C_{Na} D^{1/2} \nu^{1/2} \quad (1)$$

where I_p is the peak current (A), n is the number of electrons in the reaction ($n = 2$ for NVP), A is the active surface area of the electrode (here 4.00 cm^2 for NVP), ν is the scan rate (V s^{-1}), and C_{Na} is the concentration of Na ions in NVP (1.392×10^{-2} mol cm^{-3}). Fig. 3d shows the linear fitting profiles between the peak current density (I_p) and the square root of scan rate ($\nu^{1/2}$) from CV profiles (Fig. 3c). The oxidation and reduction currents exhibit a good linear relationship with $\nu^{1/2}$, indicating a diffusion controlled process during the sodium storage in electrodes. Through the calculation, the values of D_{Na} for the oxidation and reduction of the FSIFB assembled with the PGN/SiC/HCF anode are 8.046×10^{-13} and 1.3102×10^{-12}, respectively, indicating a faster reduction reaction.

Fig. 3e shows the EIS curves of the FSIFB assembled with the BFCF-NVP/HCF cathode and the PGN/SiC/HCF anode after 10

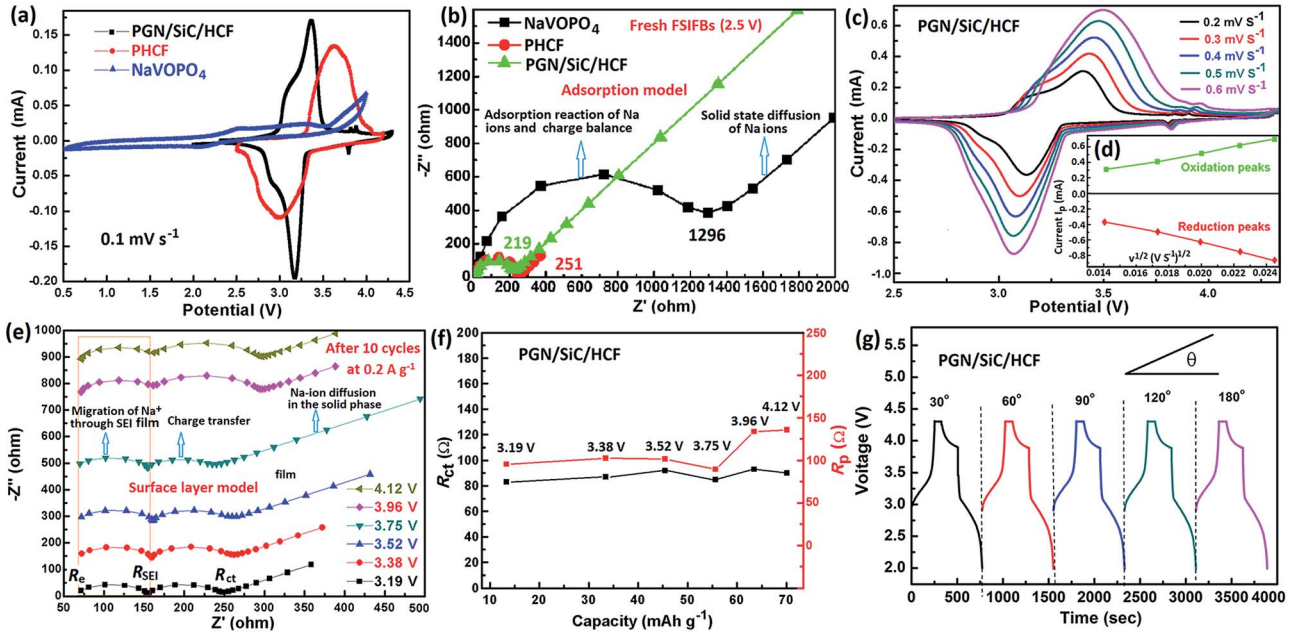

Fig. 3 Sodium-ion diffusion coefficient studies of the FSIFBs assembled with the BFCF-NVP/HCF cathode and different pre-sodiated anodes. (a) CV curves of the FSIFBs assembled with the different pre-sodiated anodes. (b) EIS curves of the fresh FSIFBs assembled with the different pre-sodiated anodes at a potential of 2.5 V. (c) CV curves of the FSIFB assembled with the PGN/SiC/HCF anode at various scan rates from 0.2 to 0.6 mV s^{-1}. (d) Corresponding linear fitting for the relationship between I_p and $v^{1/2}$ from CV profiles (c). (e) EIS curves of the FSIFB assembled with the BFCF-NVP/HCF cathode and the PGN/SiC/HCF anode after 10 cycles at different potentials at a current rate of 0.2 A g^{-1}. (f) Plots of the values of R_{ct} and R_p with the charge capacity, respectively. (g) Charge/discharge curves of the FSIFB assembled with the PGN/SiC/HCF anode at different bending angles.

cycles at different potentials at a current rate of 0.2 A g^{-1}. According to the surface layer model,[54] two depressed semicircles in the high-to-medium frequency region can be assigned to the migration of Na^+ through the solid electrolyte interphase (SEI) film (4 in Fig. 5c) and the charge transfer (2 in Fig. 5c), respectively; and the sloping lines in the low frequency region are attributed to the impedance of Na-ion diffusion in the solid phase (3 in Fig. 5c). The first semicircle (R_{SEI}, resistance of Na-ion diffusion *via* SEI film) in the high frequency region and a dot in the ultrahigh frequency region (ohmic resistance R_e, electron resistance of the active material) are almost not changed with the electrode potential, while the second semicircle (R_{ct}, resistance of charge transfer) in the medium frequency region varies with the potential significantly. The calculated values of R_{ct} and R_p (polarization resistance) are plotted with the charge capacity in Fig. 3f. It can be seen that the change of R_{ct} and R_p is small with charge capacity or potential (charging state), revealing excellent stability. Fig. 3g and 4a illustrate the charging/discharging curves of the pouch-type FSIFB assembled with the PGN/SiC/HCF anode at different bending angles and a current rate of 0.5 A g^{-1}. It can be seen that the discharge capacity of the FSIFB bent from 180° to 30° remains almost constant, revealing that the electrical stability of the fabricated FSIFB is hardly affected by external bending stress. Fig. 4b shows the charge–discharge curves of this FSIFB at 0.5 A g^{-1} before and after different bending cycles at a bending angle of 30–90°, respectively. The discharge capacity of the FSIFB is 52.6 mA h g^{-1} before bending cycles, is 35.8 mA h g^{-1} after 1600 bending cycles (Fig. 4b), and its capacity retention is 67% (ESI Fig. S4†). The aforementioned results clearly uncover the kinetics superiority of the FSIFB assembled with the BFCF-NVP/HCF cathode and the PGN/SiC/HCF anode.

Fig. 5a shows the Nyquist plots of the fresh FSIFB and the FSIFB after 12 cycles at different potentials from 100 kHz to 0.01 Hz. The Nyquist plot of the fresh FSIFB at 2.5 V is composed of a semicircle at high-frequency and a long oblique line at low-frequency, which can be explained using a simple adsorption model (Fig. 5b). The Nyquist plot of the FSIFB after 12 cycles at 2.9 V is composed of two semicircles and a long oblique line, which can be explained by the surface layer model (Fig. 5c). Fig. 5d shows the Nyquist plots of the FSIFB assembled with the BFCF-NVP/HCF cathode and the PGN/SiC/HCF anode after different cycles at 0.2 A g^{-1} and 3.17 V. All of these Nyquist plots consist of two medium-to-high frequency depressed semicircles and a low-frequency linear part. According to the SEI model,[55] the resistance (R_{SEI}) and capacitance (C_{SEI}) of the SEI film can be calculated using the following equations:

$$R_{SEI} = \rho l/S \quad (2)$$

$$C_{SEI} = \varepsilon S/l \quad (3)$$

where ρ, ε and l are the conductivity, dielectric constant and thickness of the SEI film, respectively. S is the superficial area of the electrode. If ρ, ε and S are not changed much, the increase of R_{SEI} and the decrease of C_{SEI} mean the increase of thickness (l)

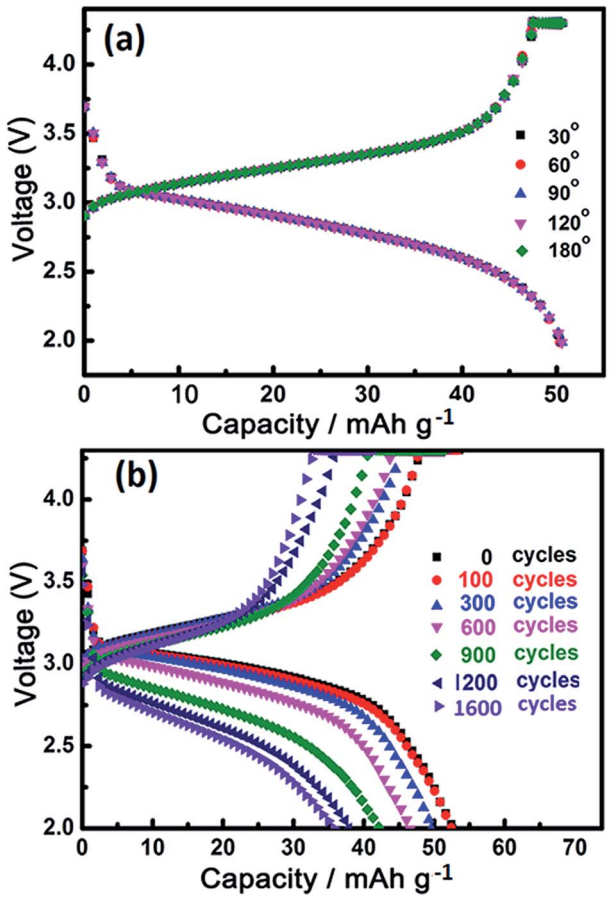

Fig. 4 (a) Charge–discharge curves of the pouch-type FSIFB assembled with the BFCF-NVP/HCF cathode and the PGN/SiC/HCF anode at 5C after bending at different angles from 180° to 30°. (b) Charge–discharge curves of this FSIFB at 0.5 A g^{-1} before and after different bending cycles at a bending angle of 30–90°.

of the SEI film. For the completely uniform SEI film, the current density (i) is given by

$$i = FD_eC_0/l \quad (4)$$

$$\frac{dl}{dt} = Ki = KFD_eC_0/l \quad (5)$$

where D_e is the diffusion coefficient of electrons in the SEI film. t is the time and when $t = 0$, $l = l_0$. C_0 is the electron concentration in the SEI film. F is the Faraday constant, and K is a constant. After integration, the following formula is obtained.

$$l = (l_0^2 + 2KFDC_0t)^{1/2} \quad (6)$$

Eqn (6) is the parabola theorem of SEI film growth. By this theory, the diffusion coefficient of electrons (D_e) and the electron concentration (C_0) in the SEI film increase with the increase of the thickness (l) of SEI film growth. In Fig. 5d the first semicircle diameter (R_{SEI}, from 83.8 to 86.4 Ω) in the high frequency region increases with the increase of the cycle number from the 2nd cycle to the 27th cycle, which means the progressive growth of the SEI film and this increased thickness is caused by the continuous deposition of Na ions. However R_{SEI} (from 86.4 to 86.6 Ω) is almost not changed with increasing the cycle number from the 27th cycle to the 36th cycle, indicating the stop of SEI film growth and the formation of an SEI film on the cycled electrode surface. The straight lines in the low frequency region of Fig. 5d represent the Warburg impedance (Z_w), which can be used to calculate the Na ion diffusion coefficient (D_{Na}) of the FSIFBs after different cycles (ESI Table S4†). The result demonstrates that the D_{Na} increases with the increase of the cycle number because of the increase of the diffusion coefficient of electrons (D_e) and the electron concentration (C_0) in the SEI film. The formation of a stable and uniform SEI film can effectively inhibit the self-discharge and the volume change of the cycled electrode, leading to a superior cycling performance (Fig. 2d and e).[56] The insertion/desertion process of Na ions in NVP may be written as

$$(1 - x)Na^+ + (1 - x)e + Na_xV_2(PO_4)_3 \leftrightarrow Na_{x3}V_2(PO_4)_3 \quad (7)$$

where x is the degree of embedded sodium. Because $Na_3V_2(PO_4)_3$ only has about two Na extraction/insertion from/into the unit structure, the maximum of x is 0.67.

The resistance of charge transfer (R_{ct}) may be written in the general form

$$R_{ct} = RT/n^2F^2c_Tk_0[M^+]^{(1-\alpha)}(1 - x)^{(1-\alpha)}x^{\alpha} \quad (8)$$

where x is the degree of embedded sodium. α is the symmetry factor of the electrochemical reaction. n is the number of electrons transferred in the electrochemical reaction. R is the molar gas constant. T is the thermodynamic temperature. k_o is the rate constant of the standard reaction. c_T is the maximum embedded concentration of Na^+ in the electrode. M^+ is the Na^+ concentration in solution. If the insertion/desertion process of Na ions in the BFCF-NVP/HCF cathode is reversible, $\alpha = 0.5$, eqn (7) can be transformed as:

$$R_{ct} = RT/n^2F^2c_Tk_0[M^+]^{0.5}(1 - x)^{0.5}x^{0.5} \quad (9)$$

According to eqn (9), when $x = 0.5$, R_{ct} has a minimal value (82 Ω at 3.19 V in Fig. 3f); when $x < 0.5$, R_{ct} increases with the decrease of x; when $x > 0.5$, R_{ct} increases with the increase of x. That is to say, R_{ct} presents an increase tendency after decrease with the increase of polarization potential of the electrode from 3.19 V to 3.52 V (Fig. 3f). Fig. 5d also shows that the second semicircle diameter (R_{ct}) in the medium frequency region at 2.9 V increases with the increase of the cycle number from the 2nd cycle to the 36th cycle significantly. These results show that the FSIFB can maintain a high degree ($x > 0.5$) of embedded sodium in the insertion/desertion cycling process of Na ions.

Fig. 5e shows the schematic of Na ion transport across the interphases and resistance contributions in the FSIFB. Fig. 5f shows the Thevenin equivalent circuit model[57] of this FSIFB. This model is comprised of an ideal voltage source, ohmic resistance (R_s) of whole reaction system and a series of branches C_n ($n = 1, 2, 3, 4, 5, 6$). V_{oc} represents the open-circuit-voltage of the cell at partial equilibrium as a function of state-of-charge

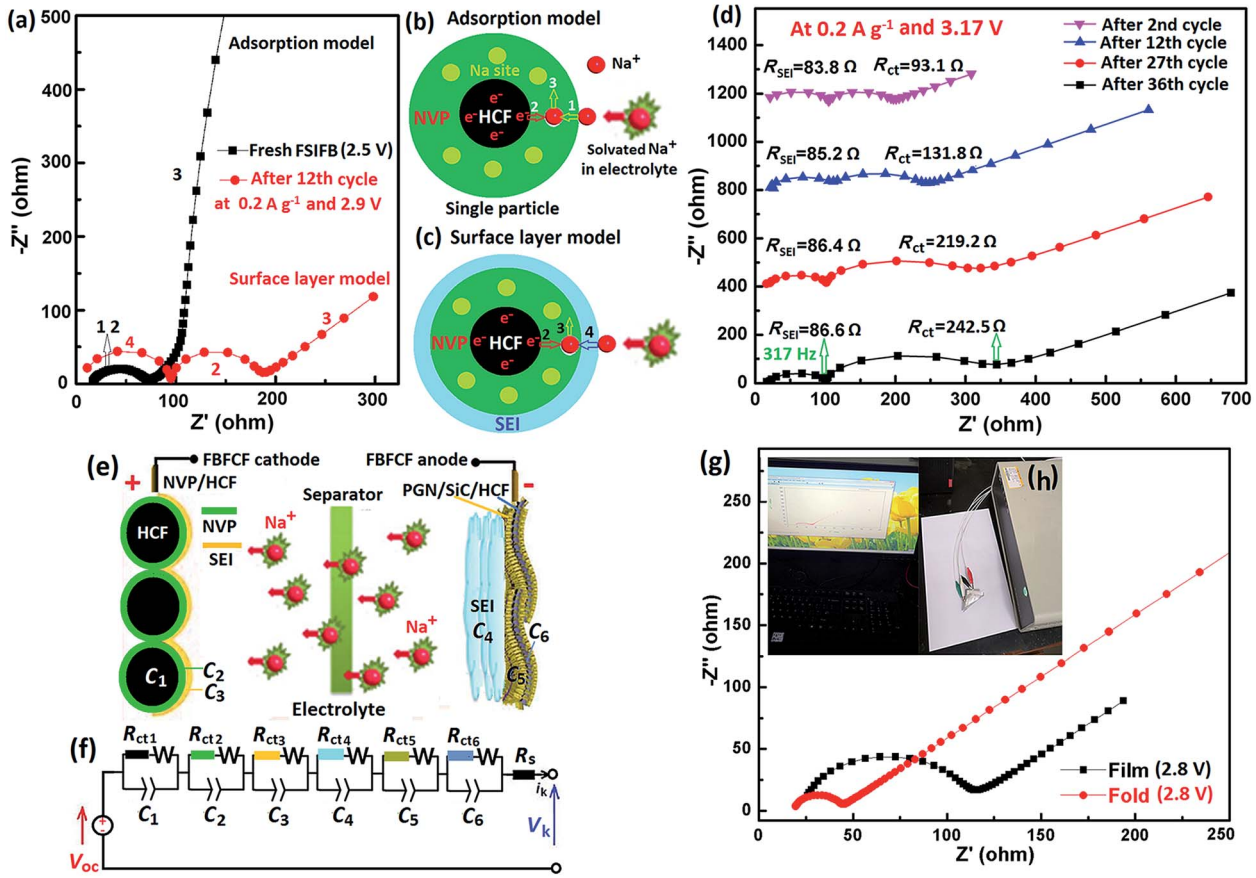

Fig. 5 (a) Nyquist plots of the FSIFB assembled with the BFCF-NVP/HCF cathode and the PGN/SiC/HCF anode after different cycles at different potentials. (b) Schematic representation of the adsorption model of a NVP/HCF single particle for the fresh FSIFB. (c) Schematic representation of the surface layer model of a NVP/HCF single particle for the FSIFB after 12th cycle. (d) EIS curves of the FSIFB assembled with the BFCF-NVP/HCF cathode and the PGN/SiC/HCF anode after different cycles at 2C and 3.17 V. (e) Schematic of Na ion transport across the interphases and resistance contributions in the FSIFB. (f) Equivalent circuit diagram of the FSIFB. (g) Nyquist plots of the FSIFB before and after being folded at a bending angle of 120° at 2C and 2.8 V. (h) EIS test photograph of the bent pouch-type FSIFB.

(SOC). According to previously published work,[58] W is the Warburg impedance which is related to the diffusion of Na ions in the solid matrix. R_{ct} corresponds to the charge-transfer resistance. R_s includes the interparticle contact resistance, electrolyte resistance and other physical resistances between the electrolyte and electrodes. V_k is the cell's terminal voltage and i_k is the throughput current. C_n is the double layer capacitance on the electrode surface. They represent the ion transport across the six interphases, such as (1) the interphase between HCF and NVP, R_{ct1} through HCF and insertion capacity (C_1), (2) the interphase between NVP and the solid electrolyte interphase (SEI), R_{ct2} through NVP and insertion capacity (C_2), (3) the interphase between the electrolyte and SEI, R_{ct3} through SEI and insertion capacity (C_3), (4) the interphase between the electrolyte and SEI, R_{ct4} through SEI and insertion capacity (C_4), (5) the interphase between the SEI and GN/SiC, R_{ct5} through GN/SiC and insertion capacity (C_5), and (6) the interphase between GN/SiC and HCF, R_{ct6} through HCF and insertion capacity (C_6). According to the Nyquist plots in Fig. 5g and h, the folded FSIFB shows a semicircle with a smaller diameter (27 Ω) than that (96 Ω) of the film FSIFB in the high-medium frequency regions. This indicates that the FSIFB flexed to desirable tension in one direction during operation has improvement in the charge-transfer characteristics due to better particle-to-particle contact in the folded electrodes at a bending angle of 120°.[59] In addition, the distance of anode/cathode electrodes in the full cell has an important influence on the resistance and the folded FSIFB may have a closer distance in the middle bending position, leading to the smaller resistance for the full cell.

To further investigate the structure change, the XRD patterns and SEM images of the BFCF-NVP/HCF cathode and the PGN/SiC/HCF anode before and after different cycles and charging at 0.5 A g^{-1} are shown in Fig. 6. The reversible insertion/desertion process of Na ions in the NVP crystal structure causes a phase transition of NVP (eqn (7)) and the formation of an SEI film. After charging, when two Na ions can desert from the $Na_3V_2(PO_4)_3$ crystal structure, rhombohedral $Na_3V_2(PO_4)_3$ is transformed into its sodium extracted phase of $NaV_2(PO_4)_3$. After discharging, when two Na ions can insert into the extracted phase, it becomes $Na_3V_2(PO_4)_3$. Therefore, in the reversible phase transition process these extracted phases all have electrochemical activity. However, some inactive

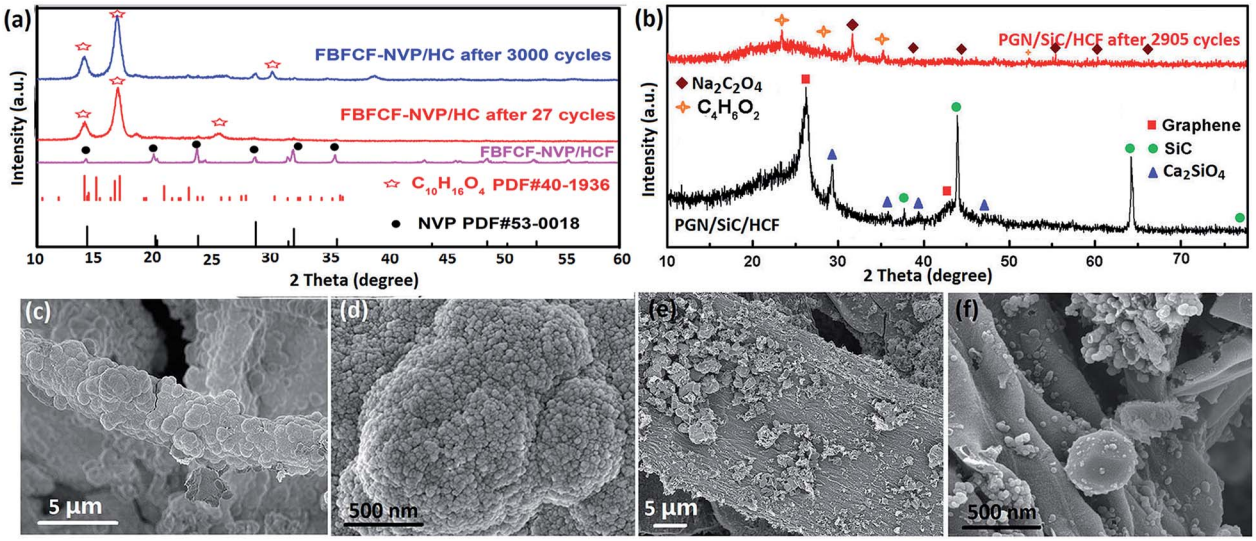

Fig. 6 (a) XRD patterns of the BFCF-NVP/HCF cathode before and after 27 and 2905 cycles at 0.5 A g^{-1}. (b) XRD patterns of the PGN/SiC/HCF anode before and after 2905 cycles and charging at 0.5 A g^{-1}. (c and d) SEM images of the BFCF-NVP/HCF cathode after 2905 cycles and charging at 0.5 A g^{-1}. (e and f) SEM images of the PGN/SiC/HCF anode after 2905 cycles and charging at 0.5 A g^{-1}.

transformation products and the SEI film were also formed with the increase of the cycle number because of the volume change and collapse of some Na sites caused by a phase change, which leads to capacity decay. As seen in Fig. 6a and b, there is significant difference in the diffraction peaks of the BFCF-NVP/HCF cathode (Fig. 6a) and the PGN/SiC/HCF anode (Fig. 6b) before and after cycles and charging. The XRD patterns of the BFCF-NVP/HCF cathode after different cycles can be well indexed to the new phase of $C_{10}H_{16}O_4$, which has a similar SEI composition to those that have been reported.[60] This could be ascribed to the formation of an SEI film on the cathode surface after cycling, and the extracted phase of NVP was covered with the SEI film. Compared with the XRD pattern after 27 cycles, the diffraction peaks in the XRD pattern after 3000 cycles have only minor changes, which shows that the structure of the SEI film formed on the surface of the BFCF-NVP/HCF cathode is stable in the charge/discharge cycles, preventing the NVP particles from peeling off. In the pre-sodiated BFCF-GN/SiC/HCF anode after 2905 cycles and charging, the strong diffraction peaks of graphene and SiC disappear, and the new phases of sodium oxalate $Na_2C_2O_4$ (JCPDS no. 49-1816) and methyl acrylate $C_4H_6O_2$ (JCPDS no. 36-1685) are formed. Furthermore, comparing the SEM images of the BFCF-NVP/HCF cathode in Fig. 6c and d with those in ESI Fig. S11,† the electrode after 2905 cycles and charging shows that the $NaVP_2O_7$ particles still tightly adhere to the HCF substrate and are connected closely with each other by conductive carbon (Fig. 6d), but obvious cracks appear in the electrode (Fig. 6c). The $NaVP_2O_7$ particles have a smaller particle size (Fig. 6d), which facilitates shortening of Na^+-ion diffusion paths and accelerates Na^+ intercalation/deintercalation. Fig. 6e shows that the pre-sodiated BFCF-GN/SiC/HCF anode after 2905 cycles and charging still maintains the morphology of HCF, and the $Na_2C_2O_4$ and $C_4H_6O_2$ nanoparticles also tightly adhere to the HCF substrate (Fig. 6f). Therefore, the HCF membrane electrode integrated with the active material and current collector is tolerant to the mechanical stress during cycling, which can keep the stable structure, and hence lead to high rate capability and cycling stability.

3.3 Electrochemical performance characterization of the sodium ion half-cells

We have successfully developed high-performance pouch-type FSIFB based on the binder-free composite film (BFCF) electrodes. The electrochemical performance of BFCF electrodes was examined in a sodium ion half-cell (SIHC) form. ESI Fig. S5† shows the electrochemical performances of the BFCF-NVP/HCF cathodes synthesized with different temperatures in the SIHC and 1 M $NaClO_4$ electrolyte (EC : PC (1 : 1, v/v) + 0% FEC). The first discharge capacities of the BFCF-NVP/HCF cathodes synthesized at 700, 750 and 800 °C at 0.1C were 74.24, 98.59, and 94.94 mA h g^{-1}, respectively. As shown in Fig. S5a–c,† the decay degree (about 18 mA h g^{-1}) of discharge capacity for the BFCF-NVP/HCF synthesized at 750 °C at current rates from 0.1C (1C = 118 mA g^{-1}) to 10C was significantly less than that (about 33 and 29 mA h g^{-1}) synthesized at 700 and 800 °C, which might have resulted from the fast electrochemical activation process in BFCF-NVP/HCF. The BFCF-NVP/HCF cathode synthesized at 750 °C not only has a flat potential plateau of 3.4 V at 0.1C (ESI Fig. S5b†), corresponding to the redox couple of V^{4+}/V^{3+},[61,62] but also showed much better rate performance during the whole cycling process, especially at high current rates (ESI Fig. S5d†). For instance, it maintained a discharge capacity of 70 mA h g^{-1} at 20C. But the BFCF-NVP/HCF cathode synthesized at 700 °C just kept a discharge capacity of 35 mA h g^{-1} at 20C (ESI Fig.-S5a†) and there's no signal for the BFCF-NVP/HCF cathode synthesized at 850 °C at 20C (ESI Fig. S5c†). ESI Fig. S6† shows the charge–discharge curves of the BFCF-NVP/HCF cathodes

synthesized with different sintering times at 750 °C, showing that the BFCF-NVP/HCF cathode synthesized with a sintering time of 8 h has a better rate capability. So the sintering time and temperature are important to determine the performance of the final electrodes.

The electrolyte additive such as fluoroethylene carbonate (FEC) also has an important influence on the electrochemical performance of SIBs.[63] Fig. 7 shows the effects of two different $NaClO_4$ electrolytes on the electrochemical performances of the BFCF-NVP/HCF cathode synthesized at 750 °C in the SIHC. The results show that the FEC electrolyte additive obviously improved the high-rate capability and long-term cycling stability of the SIHC. As shown in Fig. 7a, the BFCF-NVP/HCF cathode in the electrolyte with 5% FEC additive can deliver a super high-rate capability, showing the discharge capacities of 98.66 and 88.30 mA h g^{-1} at 20 and 50C, respectively. Even at 100 and 150C, it can also deliver the discharge capacities of 70.16 and 60.40 mA h g^{-1}, respectively, while the BFCF-NVP/HCF cathode in the electrolyte without additive (0% FEC) has only a discharge capacity of 70.0 mA h g^{-1} at 20C and almost no capacity above 20C (Fig. 7b). By comparing the CV curves of the BFCF-NVP/HCF cathode in different electrolytes (Fig. 7c), it is found that the FEC electrolyte additive can efficiently restrain the decomposition of the electrolyte component (a small reduction current peak appears near 3.3 V in the curve without FEC).[64] Through the calculation, the values of D_{Na} for oxidation and reduction in the EC : PC + 5% FEC electrolyte are 1.096×10^{-11} and 8.03×10^{-12}, respectively, while the values of D_{Na} for oxidation and reduction in the EC : PC + 0% FEC electrolyte are 7.331×10^{-12} and 2.42×10^{-12}, respectively. In addition, the BFCF-NVP/HCF cathode in the electrolyte with 5% FEC additive has better cycling stability than that in the electrolyte without additive (0% FEC) as shown in Fig. 7d. The BFCF-NVP/HCF cathode in the electrolyte with 5% FEC additive retains the capacity of 78.30 mAh g^{-1} at 20C after 150 cycles with a high capacity retention of 88.67%. Fig. 7f shows the long-term cycling stability and the coulombic efficiency of the BFCF-NVP/HCF cathode in the electrolyte with 5% FEC additive,

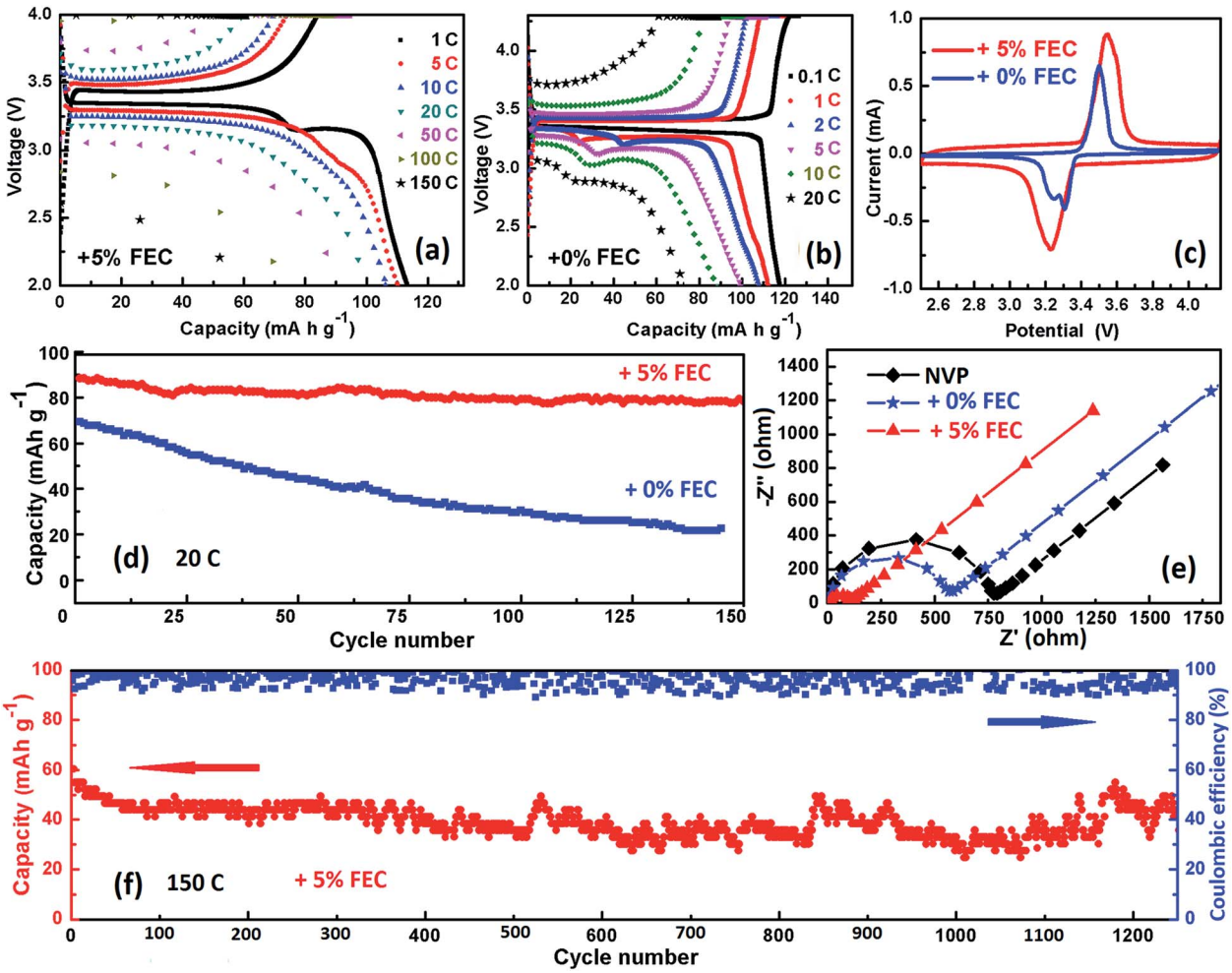

Fig. 7 Electrochemical performances of the BFCF-NVP/HCF cathode synthesized at 750 °C in the sodium ion half-cell (SIHC) form. (a) The typical charge/discharge profiles between 2.0 and 4.0 V at different rates in 1 M $NaClO_4$ electrolyte (EC : PC (1 : 1, v/v) + 5% FEC). (b) The typical charge/discharge profiles at different rates in 1 M $NaClO_4$ electrolyte (EC : PC (1 : 1, v/v) + 0% FEC). (c) CV curve profiles in different electrolytes at a scan rate of 0.1. (d) The capacity retention in different electrolytes at a 20C rate. (e) EIS curves of the different cathodes in different electrolytes. (f) The cycling performance with coulombic efficiency over 1250 cycles in 1 M $NaClO_4$ electrolyte (EC : PC (1 : 1, v/v) + 5% FEC) at a 150C rate.

which retains a capacity of 49.43 mA h g^{-1} after 1250 cycles at 150C. Fig. S5h† shows the cell with 5% FEC retains a capacity of 30.78 mA h g^{-1} after 2905 cycles at 150C, indicative of a very low capacity fading of 0.0098% per cycle. However, after 1500 cycles at 150C, its coulombic efficiency becomes unstable, due to the polarization, the decomposition of electrolyte and sodium metal, the formation of side products, and so on.[65] Fig. 7e shows the EIS curves of the fresh cathodes in different electrolytes, showing the smaller R_{ct} of the BFCF-NVP/HCF cathode in the EC : PC + 5% FEC electrolyte. ESI Fig. S7a† shows the rate capability of the BFCF-NVP/HCF cathodes synthesized at 750 °C with different coating thicknesses in SIHC and 1 M $NaClO_4$ electrolyte (EC : PC (1 : 1, v/v) + 5% FEC). The results show that the BFCF-NVP/HCF cathode with a coating thickness of 150 μm possesses the best rate capability. To understand the obtained superior electrochemical performances, more analyses of CV and EIS for the BFCF-NVP/HCF cathodes synthesized at 750 °C with a thickness of 150 μm in the EC : PC + 5% FEC electrolyte were performed (ESI Fig. S7b–d†).

The structural compositions of the hard carbon fiber (HCF) sample (ESI Fig. S8a and b†) synthesized by pyrolysis of filter paper at 750 °C for 8 h and the graphene/SiC (GN/SiC) sample (ESI Fig. S8d†) are characterized by X-ray diffraction patterns in our previous report.[47] The graphene/SiC (GN/SiC) composite nanosheets were synthesized through an *in situ* thermochemical method at 800 °C by using soda papermaking black liquor (SPBL) as a raw material. The electrochemical performance characterization of different anodes in the sodium ion half-cell (SIHC) form is shown in ESI Fig. S8c, e and S9.† The results in ESI Fig. S9a and b† show that the GN/SiC anode has poor electrochemical performances due to the formation of a solid electrolyte interface (SEI) and irreversible Na insertion into the SEI. So we used carbonized filter paper fibers decorated with GN/SiC composite nanosheets (GN/SiC/HCF) as a flexible supporting framework to prepare a BFCF anode, and the pre-sodiation of the BFCF anode was performed prior to cell fabrication to provide rich Na ions for its depassivation. The results show that the PGN/SiC/HCF anode delivers a reversible capacity of 501 mA h g^{-1} at a current rate of 10 mA g^{-1}, which is higher than that of the GN/SiC (Al) with a binder and Al current collector and the GN/SiC/HCF without pre-sodiation (ESI Fig. S9a–c†). In particular, its long cycling performance was greatly improved at a high current rate of 1 A g^{-1} due to the depassivation of the GN/SiC/HCF, showing a capacity of 234.33 mA h g^{-1} after 791 cycles with a high capacity retention of 91%, exhibiting a high coulombic efficiency (ESI Fig. S9d†).

3.4 Formation mechanism and characterization of BFCF electrodes

ESI Fig. S10† schematically illustrates the preparation processes of the NVP precursor and BFCF-NVP/HCF cathode. First, NVP powders were prepared by a sol–gel method and dispersed in *N*-methylpyrrolidone to form a slurry. Second, the slurry was coated on a filter paper spread over a glass plate, and then it was dried and sintered to form the BFCF-NVP/HCF cathode. The unique cellulose structure of filter paper was turned into a 3D conductive network framework of HCF and porous NVP was evenly coated on the HCF framework *via* the synthesis.

X-ray diffraction (XRD), Raman spectroscopy, N_2 adsorption and desorption isotherm measurements, scanning electron microscopy (SEM) and energy dispersive spectroscopy (EDS) of the BFCF-NVP/HCF cathodes synthesized at different temperatures were performed to investigate their composition and structure (Fig. 8). As shown in Fig. S10,† the XRD patterns of the BFCF-NVP/HCF synthesized at different temperatures all exhibit the same diffraction peaks as the NVP/C blank sample (Fig. 8a), corresponding to a rhombohedral NASICON structure of NVP with JCPDS card no. 53-0018.[46] The Raman spectrum (Fig. 8b) and the deconvoluted Raman spectrum (Fig. 8c) of the BFCF-NVP/HCF cathode synthesized at 750 °C reveal the D band

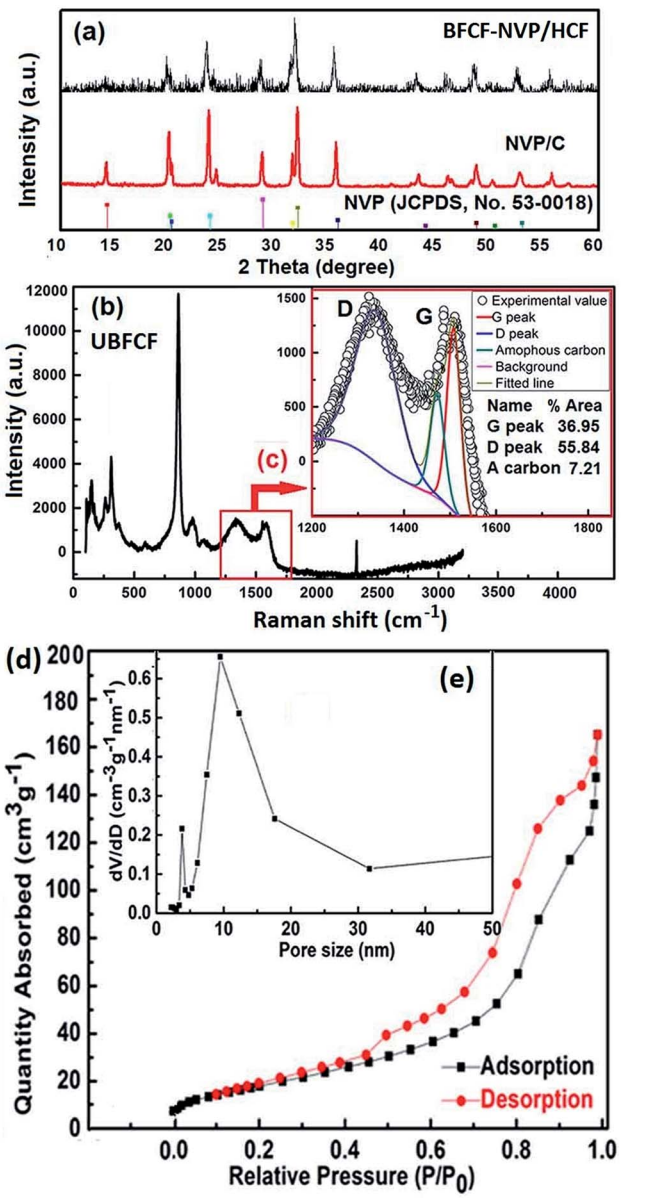

Fig. 8 Structural characterization of the BFCF-NVP/HCF samples synthesized at 750 °C: (a) XRD patterns, (b and c) Raman spectra, (d) N_2 adsorption and desorption isotherm and (e) pore size distribution.

(1347 cm^{-1}) and G band (1590 cm^{-1}) with a ratio of $I_D/I_G = 1.19$, indicating that the carbon in the BFCF-NVP/HCF is disordered hard carbon.[66] The pore structure of the BFCF-NVP/HCF synthesized at 750 °C was elucidated by nitrogen adsorption–desorption isotherms. Fig. 8d shows the type-IV adsorption–desorption isotherm and distinct H3-type hysteresis, indicating the existence of uneven slit-shaped holes. Fig. 8e shows that the pore-size distribution of the BFCF-NVP/HCF is in the range of mesopores (5–30 nm). The mesoporous structure of the BFCF-NVP/HCF can also be observed from the SEM image in Fig. S12f.†

The morphology of the BFCF-NVP/HCF cathode synthesized at 750 °C is shown in Fig. S12,† displaying the core/shell structure of porous NVP coated highly conductive hard carbon fibers. The accurate carbon content in the BFCF-NVP/HCF synthesized at 750 °C was determined using a Vario EL III CHN elemental analyzer (ESI Table S5†). The results show that the mass ratio of NVP : HCF in the BFCF-NVP/HCF is 55.6 : 44.4. In this work, the total mass of the BFCF-NVP/HCF is 4.5 mg, so the actual mass loading of NVP active material is about 2.34 mg cm^{-2}, which is much higher than that in a traditional electrode supported on Al foil (NVP/C@Al, about 1.6 mg cm^{-2}).[65] The high loading of NVP active material is beneficial to obtain high volume specific capacity in the cell. The high resolution transmission electron microscopy (HRTEM) images (ESI Fig. S13†) of the BFCF-NVP/HCF sample synthesized at 750 °C show that the core diameter of single HCF is about 60 nm, and the thickness of the NVP shell is about 30 nm. Moreover, the selected area electron diffraction (SAED) patterns in ESI Fig. S13g and h† show that some NVP crystal particles have a super lattice structure with the different interplanar spacings, which indicates that HCF can induce the nucleation and growth of NVP crystal particles and form a super lattice structure in the synthesis. The super lattice structure has abundant reactive sites of electrons and Na^+ in the quantum wells due to quantum confinement and size effects.[66]

4. Conclusions

In summary, we have successfully prepared flexible and binder-free composite film (BFCF) electrodes without using conductive carbon and current collectors for cheap flexible sodium-ion full batteries (FSIFBs). This BFCF is supported on a carbonized filter paper fiber matrix with an effectively conductive 3D network. The 5% fluoroethylene carbonate (FEC) electrolyte additive obviously improved the rate performance of the BFCF cathode based on porous $Na_3V_2(PO_4)_3$ (NVP) coated hard carbon fibers (HCF). Even at a super high-rate of 150C (equivalent to discharge within 24 seconds), it can also deliver a discharge capacity of 60.40 mA h g^{-1}, which is maintained at 30.78 mA h g^{-1} after 2903 cycles. Pre-sodiated BFCF anodes can significantly increase its reversible capacity and rate capacity. The pre-sodiated graphene/SiC/HCF (PGN/SiC/HCF) anode gives a highly reversible capacity of 501 mA h g^{-1} at 10 mA g^{-1} and an excellent rate capacity of up to 100 mA h g^{-1} at 20 A g^{-1}. After 791 cycles, it can still maintain a discharge capacity of 234.33 mA h g^{-1} at a high current rate of 1 A g^{-1}. More importantly, compared with traditional electrodes supported on Al foil, the optimized FSIFB assembled with the BFCF-NVP/HCF cathode and the PGN/SiC/HCF anode delivers both high-output voltage (3.34 V) and high energy density (234.1 W h kg^{-1} at a high-rate of 0.5 A g^{-1}), ultralong cyclability (over 2905 cycles at 0.5 A g^{-1} and 1000 cycles at 5 A g^{-1}) and high coulombic efficiency (approaching 100%). Unexpectedly, the electrochemical performances of the FSIFB were not influenced when the battery was under various bending and twisting conditions. A discharge capacity of 35.8 mA h g^{-1} was achieved for this FSIFB after 1600 bending cycles at a bending angle of 30–90° at 0.5 A g^{-1}, and its capacity retention is 67%, which has not been reported. This work provides an effective way to develop flexible sodium-ion batteries by using bendable, low-cost electrode materials with excellent electrochemical performances.

Conflicts of interest

There are no conflicts to declare.

Acknowledgements

The authors thank the National Natural Science Foundation of China (Grant No. 51672139, 51472127 and 51272144) for the financial support.

Notes and references

1 B. Luo, D. L. Ye and L. Z. Wang, *Adv. Sci.*, 2017, **4**, 1700104.
2 B. Luo, Y. Hu, X. Zhu, T. Qiu, L. Zhi, M. Xiao, H. Zhang, M. Zou, A. Cao and L. Z. Wang, *J. Mater. Chem. A*, 2018, **6**, 1462.
3 Y. Hu, B. Luo, D. Ye, X. Zhu, M. Lyu and L. Z. Wang, *Adv. Mater.*, 2017, **29**, 1606132.
4 T. Dhawa, S. Chattopadhyay, G. De and S. Mahanty, *ACS Omega*, 2017, **2**, 6481–6491.
5 S. Chattopadhyay, S. Maiti, I. Das, S. Mahanty and G. De, *Adv. Mater. Interfaces*, 2016, **3**, 1600761.
6 G. Zhou, F. Li and H.-M. Cheng, *Energy Environ. Sci.*, 2014, **7**, 1307.
7 L. Li, Z. Wu, S. Yuan and X.-B. Zhang, *Energy Environ. Sci.*, 2014, **7**, 2101.
8 G. Wu, P. Tan, X. Wu, L. Peng, H. Cheng, C. F. Wang, W. Chen, Z. Y. Yu and S. Chen, *Adv. Funct. Mater.*, 2017, **27**, 1702493.
9 X. Wang, X. Lu, B. Liu, D. Chen, Y. Tong and G. Shen, *Adv. Mater.*, 2014, **26**, 4763.
10 L. Hu, H. Wu, F. Mantia, Y. Yang and Y. Cui, *ACS Nano*, 2010, **4**, 5843.
11 W. Liu, B. Shi, Y. Wang, Y. Li, H. Pei, R. Guo, X. Hou, K. Zhu and J. Xie, *ChemistrySelect*, 2018, **3**, 5608.
12 F. Li, G. Zhai, H. Ren, G. Wang and H. Wang, *Ionics*, 2018, **24**, 111.
13 L. Hu, M. Pasta, F. L. Mantia, L. Cui, S. Jeong, H. D. Deshazer, J. W. Choi, S. M. Han and Y. Cui, *Nano Lett.*, 2010, **10**, 708.
14 L. Liu, W. Ma and Z. Zhang, *Small*, 2011, **7**, 1504.

15 B. Liu, X. Wang, B. Liu, Q. Wang, D. Tan, W. Song, X. Hou, D. Chen and G. Shen, *Nano Res.*, 2013, **6**, 525.
16 B. Liu, X. Wang, H. Chen, Z. Wang, D. Chen, Y.-B. Cheng, C. Zhou and G. Shen, *Sci. Rep.*, 2013, **3**, 1622.
17 J. S. Park, J. Kim, J. H. Jo, S. T. Myung and T. Rojo, *J. Mater. Chem. A*, 2018, **6**, 16627.
18 Y. Lee, J. K. Yoo, Y. Oh, H. Park, W. Go, S. T. Myung and J. Kim, *J. Mater. Chem. A*, 2018, **6**, 17571.
19 H. Wang, S. Yuan, D. Ma, X. Zhang and J. Yan, *Energy Environ. Sci.*, 2015, **8**, 1660.
20 S. Xu, Y. Zhao, S. Liu, X. Ren, L. Chen, W. Shi, X. Wang and D. Zhang, *J. Mater. Sci.*, 2018, **53**(17), 12334.
21 F. Bella, A. B. Muñoz-García, F. Colò, G. Meligrana, A. Lamberti, M. Destro, M. Pavone and C. Gerbaldi, *ACS Omega*, 2018, **3**, 8440.
22 C. Yuan, Q. Wu, Q. Li, Q. Duan, Y. Li and H. Wang, *ACS Sustainable Chem. Eng.*, 2018, **6**, 8392–8399.
23 F. Bella, F. Colý, J. R. Nair and C. Gerbaldi, *ChemSusChem*, 2015, **8**(21), 3668.
24 F. Colo, F. Bella, J. R. Nair and C. Gerbaldi, *J. Power Sources*, 2017, **365**, 293.
25 J. Y. Hwang, S. T. Myung and Y. K. Sun, *Chem. Soc. Rev.*, 2017, **46**, 3529.
26 W. Ren, Z. Zhu, Q. An and L. Mai, *Small*, 2017, **23**, 1604181.
27 W. Wang, Q. Xu, H. Liu, Y. Wang and Y. Xia, *J. Mater. Chem. A*, 2017, **5**, 8440.
28 D. Guo, J. Qin, Z. Yin, J. Bai, Y. Sun and M. Cao, *Nano Energy*, 2018, **45**, 136.
29 W. Song, X. Ji, Z. Wu, Y. Zhu, Y. Yang, J. Chen, M. Jing, F. Li and C. E. Banks, *J. Mater. Chem. A*, 2014, **2**, 5358.
30 D. Xu, D. Chao, H. Wang, Y. Gong, R. Wang, B. He, X. Hu and H. Fan, *Adv. Energy Mater.*, 2018, **8**, 1702769.
31 Q. Ni, Y. Bai, Y. Li, L. Ling, L. Li, G. Chen, Z. Wang, H. Ren, F. Wu and C. Wu, *Small*, 2018, **14**, 1702864.
32 Y. Jiang, X. Zhou, D. Li, X. Cheng, F. Liu and Y. Yu, *Adv. Energy Mater.*, 2018, **8**, 1800068.
33 C. Zhu, P. Kopold, P. A. van Aken, J. Maier and Y. Yu, *Adv. Mater.*, 2016, **28**, 2408.
34 H. Hou, X. Qiu, W. Wei, Y. Zhang and X. Ji, *Adv. Energy Mater.*, 2017, **7**, 1602898.
35 J. Yang, X. Zhou, D. Wu, X. Zhao and Z. Zhou, *Adv. Mater.*, 2017, **29**, 1604108.
36 X. Xiong, C. Yang, G. Wang, Y. Lin, X. Ou, J.-H. Wang, B. Zhao, M. Liu, Z. Lin and K. Huang, *Energy Environ. Sci.*, 2017, **10**, 1757.
37 I. Izanzara, M. Dahbi, M. Kiso, S. Doubaji, S. Komaba and I. Saadoune, *Carbon*, 2018, **137**, 165.
38 Z. Li, Z. Jian, X. Wang, I. A. Rodríguez-Pérez, C. Bommier and X. Ji, *Chem. Commun.*, 2017, **53**, 2610.
39 Y.-E. Zhu, L. Yang, X. Zhou, F. Li, J. Wei and Z. Zhou, *J. Mater. Chem. A*, 2017, **5**, 9528.
40 L. Xiao, H. Lu, Y. Fang, M. L. Sushko, Y. Cao, X. Ai, H. Yang and J. Liu, *Adv. Energy Mater.*, 2018, **8**, 1703238.
41 Y. Zheng, Y. Wang, Y. S. Lu, Y. S. Hu and J. Li, *Nano energy*, 2017, **39**, 489.
42 N. Zhang, Q. Liu, W. Chen, M. Wan, X. Li, L. Wang, L. Xue and W. Zhang, *J. Power Sources*, 2018, **378**, 331.
43 B. Xiao, F. A. Soto, M. Gu, K. S. Han, J. Song, H. Wang, M. H. Engelhard, V. Murugesan, K. T. Mueller, D. Reed, V. L. Sprenkle, P. B. Balbuena and X. Li, *Adv. Energy Mater.*, 2018, **8**, 1801441.
44 L. Chen, Y. Zhao, S. Liu and L. Zhao, *ACS Appl. Mater. Interfaces*, 2017, **9**, 44485–44493.
45 P. Barpanda, L. Lander, S. Nishimura and A. Yamada, *Adv. Energy Mater.*, 2018, **8**, 1703055.
46 W. Ren, X. Yao, C. Niu, Z. Zheng, K. Zhao, Q. An, Q. Wei, M. Yan, L. Zhang and L. Mai, *Nano Energy*, 2016, **28**, 216.
47 X. Yi, Y. Zhang, W. He, X. Zhang, G. Yang, Z. Wang, Y. Wang and Q. Chen, *ChemElectroChem*, 2017, **6**, 1320.
48 H. G. Zhang, H. Ning, J. Busbee, Z. H. Shen, C. Kiggins, Y. Hua, J. Eaves, J. Davis, T. Shi, Y. T. Shao, J. M. Zuo, X. H. Hong, Y. Chan, S. B. Wang, P. Wang, P. C. Sun, S. Xu, J. Liu and P. V. Braun, *Sci. Adv.*, 2017, **3**, e1602427.
49 B. Liu, J. Zhang, X. F. Wang, G. Chen, D. Chen, C. W. Zhou and G. Z. Shen, *Nano Lett.*, 2012, **12**, 3005.
50 Y. Yang, G. H. Yu, J. J. Cha, H. Wu, M. Vosgueritchian, Y. Yao, Z. A. Bao and Y. Cui, *ACS Nano*, 2011, **5**, 9187.
51 S. Kobayashi and Y. Uchimoto, *J. Phys. Chem. B*, 2005, **109**, 13322.
52 F. Le Normand, J. Hommet, T. Szörényi, C. Fuchs and E. Fogarassy, *Phys. Rev. B: Condens. Matter Mater. Phys.*, 2001, **64**, 235416.
53 J. Wang, Z. Wang, X. Li, H. Guo, X. Wu, X. Zhang and W. Xiao, *Electrochim. Acta*, 2013, **87**, 224.
54 M. Tomas, P. G. Bruce and J. B. Goodenough, *J. Electrochem. Soc.*, 1985, **132**, 1521.
55 F. Orsini, M. Dolle and J.-M. Tarascon, *Solid State Ionics*, 2000, **135**, 213.
56 S. Nejad, D. T. Gladwin and D. A. Stone, *J. Power Sources*, 2016, **316**, 183.
57 B. Yan, X. Li, Z. Bai, Y. Zhao, L. Dong, X. Song, D. Li, C. Langford and X. Sun, *Nano Energy*, 2016, **24**, 32.
58 A. M. Gaikwad, H. N. Chu, R. Qeraj, A. M. Zamarayev and D. A. Steingart, *Energy Technol.*, 2013, **1**, 177.
59 M. Pivko, I. Arcon, M. Bele, R. Dominko and M. Gaberscek, *J. Power Sources*, 2012, **216**, 145.
60 C. Vidal-Abarca, P. Lavela, J. L. Tirado, A. V. Chadwick, M. Alfredsson and E. Kelder, *J. Power Sources*, 2012, **197**, 314.
61 L. S. Plashnitsa, E. Kobayashi, Y. Noguchi, S. Okada and J.-I. Yamaki, *J. Electrochem. Soc.*, 2010, **157**, A536.
62 R. Dugas, B. Zhang, P. Rozier and J. M. Tarascona, *J. Electrochem. Soc.*, 2016, **163**, A867.
63 S. S. Zhang, K. Xu and T. R. Jow, *J. Power Sources*, 2006, **160**, 1349.
64 S. Liu, S. Tang, X. Zhang, A. Wang, Q. H. Yang and J. Luo, *Nano Lett.*, 2017, **17**, 5862.
65 L. L. Zhang, L. Zhen, X. L. Yang, X.-K. Ding, Y.-X. Zhou, H.-B. Sun, H.-C. Tao, L. Y. Xiong and Y. H. Huang, *Nano Energy*, 2017, **34**, 111.
66 Z. Wang, W. He, X. Zhang, Y. Yue, G. Yang, X. Yi, Y. Wang and J. Wang, *ChemElectroChem*, 2017, **4**, 671.